Advanced Functional Materials

ADVANCED FUNCTIONAL MATERIALS
www.afm-journal.de

RESEARCH ARTICLE OPEN ACCESS

Fullerene-Mediated Iodine Immobilization at Buried Interfaces in Sn–Pb Perovskite Solar Cells

Chi-Jing Huang[1] | Yi-Sheng Lin[1] | Matyas Daboczi[2] | Yueyao Dong[3] | Anuj Kumar Singh[4] | Luis Lanzetta[4] | Yun-Shan Li[1] | Chang-Hao Wang[1] | Huan-Wei Lin[1] | Wei-Jia Qiu[5] | Yi-Ting He[6] | Chun-Fu Chang[6] | Sanjayan Sathasivam[7] | Derya Baran[4] | Thomas J. Macdonald[3] | Chieh-Ting Lin[1,5,8]

[1]Department of Chemical Engineering, National Chung Hsing University, Taichung, Taiwan | [2]HUN-REN Centre for Energy Research, Institute of Technical Physics and Materials Science, Budapest, Hungary | [3]Department of Electronic and Electrical Engineering, University College London, London, UK | [4]Material Science and Engineering Program (MSE), Physical Science and Engineering Division (PSE), King Abdullah University of Science and Technology (KAUST), Thuwal, Saudi Arabia | [5]Graduate Program in Semiconductor and Green Technology, Academy of Circular Economy, National Chung Hsing University, Nantou City, Nantou County, Taiwan | [6]Department of Applied Chemistry, National Yang Ming Chiao Tung University, Hsinchu, Taiwan | [7]School of Engineering, London South Bank University, London, UK | [8]Innovation and Development Center of Sustainable Agriculture, National Chung Hsing University, Taichung City, Taiwan

Correspondence: Chieh-Ting Lin (c.lin15@nchu.edu.tw)

Received: 11 April 2026 | **Revised:** 16 July 2026 | **Accepted:** 4 August 2026

Keywords: buried interface | hole selectivity | ICBA | interfacial recombination | iodine suppression | perovskite | p-i-n structure

ABSTRACT

Narrow-bandgap perovskite solar cells (PSCs) are promising absorbers for tandem photovoltaics; however, their performance remains limited by interfacial recombination and instability, particularly Sn^{2+} oxidation and halide-related degradation. Although fullerene derivatives have been explored as charge-selective interlayers, their mechanistic role in regulating buried-interface chemistry remains unclear. Herein, we demonstrate that indene-C_{60} bisadduct (ICBA) functions as an electronic and chemical regulator in inverted (p-i-n) PSCs. When introduced via precursor additive engineering, ICBA preferentially accumulates at the buried perovskite/HTL interface, where its ambipolar, weakly electron-selective character suppresses undesired electron extraction while electronically modifying the buried perovskite surface to preserve hole extraction. More importantly, spectroscopic and morphological analyses reveal that ICBA interacts with iodine species and mitigates Sn^{2+} oxidation during thermal annealing. This dual interfacial regulation reduces trap formation and energetic disorder, enhances photoluminescence and carrier lifetimes, and improves stability. Devices incorporating ICBA achieve a peak power conversion efficiency of 22.7% and retain over 93% of their efficiency after 2496 h of dark storage, compared with 81% for reference devices. These findings establish a chemically informed buried-interface stabilisation strategy for improving the performance and durability of lead-reduced perovskite photovoltaics.

1 | Introduction

Metal halide perovskite solar cells (PSCs) have rapidly emerged as a leading photovoltaic technology due to their high-power conversion efficiencies (PCEs), solution-processability, and low-cost fabrication potential [1–3]. Among them, narrow-bandgap mixed tin-lead (Sn-Pb) perovskites have attracted particular interest as promising absorbers for all-perovskite tandem solar cells, owing

Chi-Jing Huang and Yi-Sheng Lin contributed equally to this work.

to their ability to harvest near-infrared light and their tunable optoelectronic properties [4–8]. Despite these advantages, the instability caused by Sn^{2+} oxidation of Sn–Pb perovskite devices remains a major challenge impeding commercialization [5, 9–11].

A key degradation pathway in Sn–Pb and Sn-based perovskites is the spontaneous formation of molecular iodine (I_2) under thermal, electrical, or light-induced stress [12–14]. I_2 accelerates the oxidation of Sn^{2+} to Sn^{4+} and diffuses into interfacial layers, where it can trigger undesirable chemical reactions and increase non-radiative recombination [13]. While the chemical role of I_2 in Sn-Pb degradation is well documented, far less attention has been paid to the spatial aspects of this process, particularly its impact at the buried interface. In typical p-i-n structured devices, the buried interface refers to the contact between the transparent bottom electrode, hole transport layer (HTL), and perovskite absorber [15–17]. As this interface is located on the light-incident side and plays a critical role in hole extraction, it is subject to intense photo-induced and electrical stress. However, the vulnerability of the buried interface to I_2-induced degradation remains largely unexplored, even though this process can accelerate efficiency losses through rapid burn-in during early operation and through Sn^{4+} formation already initiated in fresh films during fabrication [13, 14]. In addition to iodine-related pathways, the acidic and hygroscopic nature of PEDOT:PSS further accelerates interfacial degradation at the buried contact, underscoring the urgent need for interface engineering strategies that can simultaneously address these chemical instability pathways.

Among these degradation routes, iodine-induced processes have received particular attention. Recent studies have demonstrated that certain fullerene derivatives, such as C_{60} and 6, 6-phenyl-C_{61}-butyric acid methyl ester (PCBM), can effectively scavenge iodine species through Lewis acid-base interactions [18]. Acting as soft Lewis acids, these fullerenes form stable charge-transfer complexes with diffused I_2 or I_3^-, thereby mitigating iodine-induced degradation at perovskite interfaces. However, these approaches have been primarily explored in Pb-based perovskite systems, with fullerenes typically deposited on the perovskite top surface, serving as electron transport layers or interface modifiers at the top interface [18]. Interestingly, this iodine scavenging capability arises primarily from the soft Lewis nature of fullerenes rather than from their lowest unoccupied molecular orbital (LUMO) levels or electron extraction behavior; suggesting that chemical stabilization can be achieved independently of energy level alignment [18].

Although this finding decouples iodine stabilization from energy-level considerations, the electronic properties of fullerene materials remain critical for interfacial charge selectivity in photovoltaic devices [19]. In inverted (p-i-n) architectures, where light enters through the transparent bottom electrode (typically ITO), the buried interface not only serves as the chemical front line for I_2-induced degradation but also plays a pivotal role in hole extraction [20–23]. In such a configuration, the interface-modifying material must meet dual requirements: chemically suppressing I_2-induced degradation while simultaneously enabling selective hole transport and preventing undesired electron extraction. While fullerenes, such as C_{60} and PCBM, are chemically advantageous and widely used for their excellent electron mobility, their energy levels present key limitations at the buried interface in p-i-n perovskite solar cells. Their low LUMO promotes undesired electron trapping and recombination [19, 24, 25], while their deep highest occupied molecular orbital (HOMO) creates a barrier for hole transfer, collectively impairing device performance [26].

Although fullerene derivatives have been widely explored as electron transport materials in organic and perovskite photovoltaics, their mechanistic role at the buried hole-collecting interface of Sn-Pb perovskites remains largely unexplored. Here, we demonstrate that ICBA functions not merely as an additive, but as a dual electronic and chemical regulator that selectively improves hole extraction while scavenging iodine species, thereby mitigating Sn^{2+} oxidation and interfacial recombination. Although ICBA is commonly employed as an electron-transport material, its charge transport is ambipolar rather than exclusively electron-selective [27]. Its relatively shallow electron affinity lies outside the reported trap-free electron-transport window, resulting in weaker electron transport than PCBM and C_{60} [26]. Recent studies have also demonstrated appreciable hole transport and enhanced hole extraction following ICBA modification at perovskite interfaces [27]. These characteristics make ICBA attractive for a hole-collecting buried interface, where undesired electron extraction should be suppressed without substantially impeding hole collection. At the same time, ICBA exhibits a strong chemical affinity toward molecular iodine (I_2), allowing it to act as a scavenger that mitigates I_2-induced Sn^{2+} oxidation. During film formation, ICBA spontaneously accumulates at the buried interface, providing passivation and energy-level alignment without additional layers. Through this dual role of suppressing iodine- and PEDOT:PSS-related degradation while improving charge-transfer selectivity, ICBA significantly enhances the stability and performance of inverted Sn-Pb perovskite devices and establishes a precursor-driven buried-interface engineering strategy for next-generation narrow-bandgap solar cells [19, 24–26].

2 | Results and Discussion

2.1 | Energy Level Alignment and Carrier Transport Behavior of Fullerene Additives

To identify a suitable fullerene derivative for precursor engineering, we first compared the intrinsic electronic and carrier-selective characteristics of C_{60}, PCBM, and ICBA, whose molecular structures are shown in Figure 1a. Their HOMO levels were experimentally determined using ambient-pressure photoemission spectroscopy (APS) (Figures S1 and S2), while the LUMO levels were estimated by combining the measured HOMO values with the corresponding optical bandgaps. The shallower LUMO level of ICBA (−3.5 eV) compared to those of PCBM (−3.7 eV) and C_{60} (−4.3 eV) is expected to block undesired electron extraction at the HTL/perovskite interface. Additionally, the HOMO levels of all three fullerene derivatives are deeper than the valence band maximum of the Sn-Pb perovskite (−5.7 eV), indicating that direct hole transfer into the fullerene phase is not energetically favored. However, the offset is smallest for ICBA, at approximately 0.1 eV, whereas PCBM and C_{60} introduce larger energetic barriers. These intrinsic energy levels are therefore used primarily as a qualitative criterion for comparing the fullerene derivatives, rather than as evidence that holes are transported through a

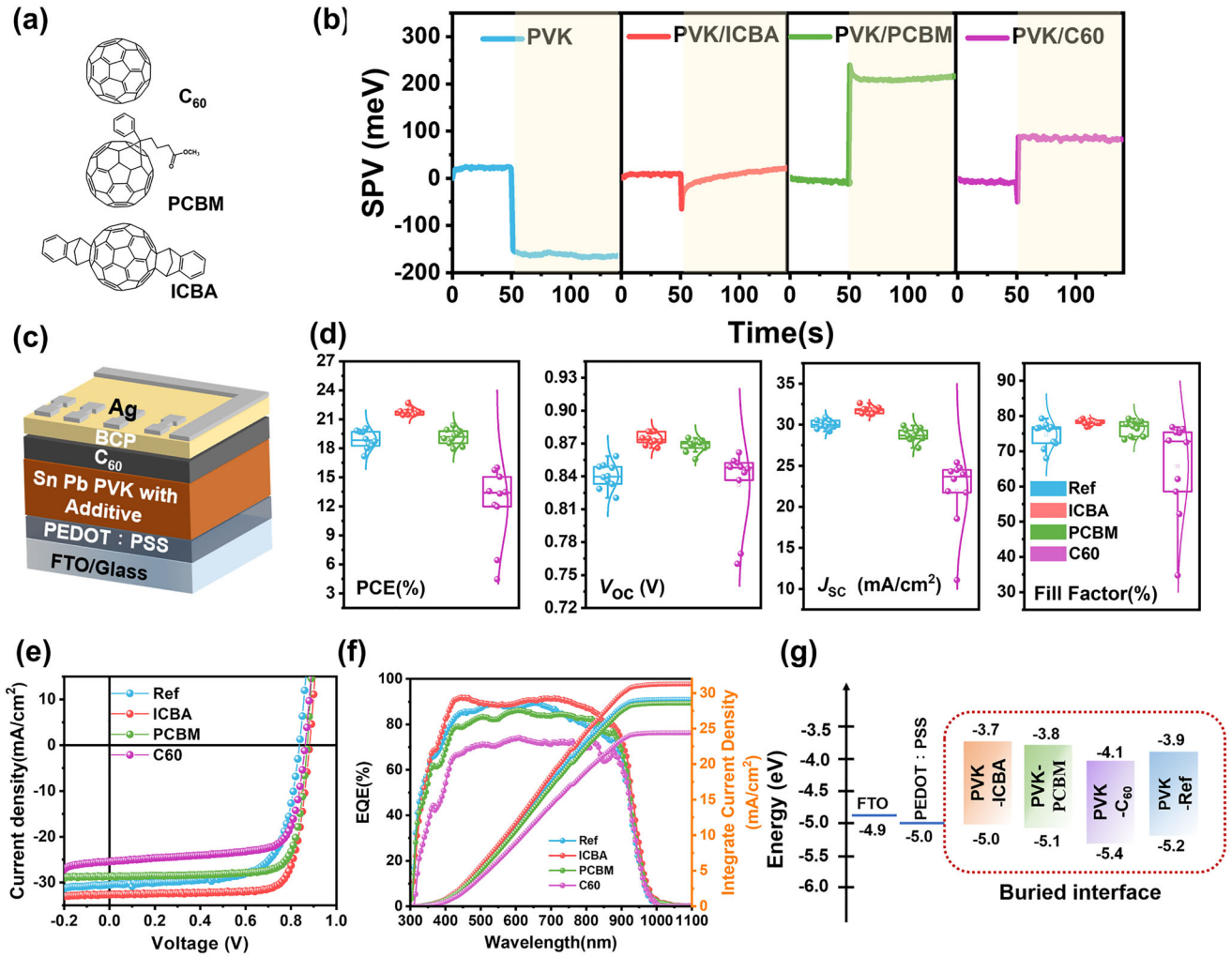

FIGURE 1 | (a) Chemical structures of the fullerene derivatives: C_{60}, PCBM, and ICBA. (b) Surface photovoltage (SPV) response of perovskite films with various fullerene interlayers under white-light illumination. The shaded (yellow) regions indicate the illumination intervals. SPV is defined here as the difference between the surface potential measured under illumination (ϕ_{ill}) and that under dark (ϕ_{dark}) conditions: SPV = ϕ_{ill}—ϕ_{dark}. (c) Schematic of the fabricated PSC. (d) Statistical distribution of the photovoltaic parameters (V_{OC}, J_{SC}, FF, and PCE) for devices using fullerene additives in the precursor solution. (e) Current density-voltage (*J*–*V*) characteristics for devices integrated with different fullerene derivatives. (f) External quantum efficiency (EQE) spectra and integrated current densities of the corresponding devices. (g) Energy-level alignment at the PEDOT:PSS/perovskite with fullerene additives buried interface, derived from APS measurements on the peeled buried surface of the perovskite films.

continuous fullerene layer. Among the three materials, ICBA provides the smallest HOMO offset together with the shallowest LUMO, making it the least disruptive to hole collection while more effectively suppressing undesired electron transfer. The actual electronic modification of the buried interface following precursor incorporation is examined directly below.

To further investigate the carrier selectivity of different fullerene materials, we conducted surface photovoltage (SPV) measurements using a test structure in which fullerenes were coated on top of the glass/perovskite layer (Figure 1b). Under these conditions, a positive SPV signal indicates an increased density of photoexcited electrons at the surface of the fullerene (i.e., electron extraction from the perovskite photoactive layer), whereas a negative signal suggests hole extraction or suppressed electron transfer [28, 29]. As expected, based on the energy-level measurements, C_{60} and PCBM yielded strong positive SPV responses, confirming their characteristic electron-extraction behavior. In contrast, the ICBA-coated sample displayed a brief negative signal, followed by a minimal net change, indicating that ICBA does not efficiently extract electrons from the perovskite. This behavior is consistent with the relatively shallow electron affinity of ICBA, which lies outside the reported trap-free electron-transport window and results in more trap-limited electron transport than PCBM and C_{60} [26]. Recent studies have also highlighted the ambipolar transport characteristics of ICBA and its ability to support hole extraction following interfacial modification [27]. Although the SPV response alone does not directly demonstrate hole transport, it shows that ICBA is less prone to undesired electron extraction, which is advantageous at the hole-collecting buried interface of p-i-n devices(Figure 1c).

To identify where fullerene derivatives exert their influence within the device architecture, we compared configurations in which fullerene layers were positioned either beneath the perovskite layer (buried interface) or on top of the perovskite

TABLE 1 | The reported photovoltaic parameters represent the average values obtained from a sample of 10 devices. The best-performing device is in bold font.

	Efficiency (%)	V_{OC} (V)	Fill factor (%)	J_{SC} (mA cm^{-2})
Ref	18.9 ± 1.0 **(20.1)**	0.84 ± 0.01 **(0.84)**	74.7 ± 0.4 **(77.5)**	30.1 ± 0.5 **(30.9)**
ICBA	21.8 ± 0.4 **(22.7)**	0.87 ± 0.01 **(0.88)**	78.3 ± 0.6 **(78.8)**	31.8 ± 0.4 **(32.6)**
PCBM	19.2 ± 0.8 **(19.8)**	0.87 ± 0.01 **(0.87)**	76.6 ± 2.1 **(79.3)**	28.8 ± 0.8 **(28.7)**
C_{60}	12.2 ± 3.8 **(16.0)**	0.83 ± 0.04 **(0.86)**	65.7 ± 13.9 **(73.0)**	22.0 ± 4.3 **(25.4)**

layer (top-side). As shown in Figure S3 and Tables S1,S2, devices incorporating a buried fullerene layer exhibited significantly higher efficiencies compared with those with top-side deposition, which displayed a markedly different performance trend. These observations indicate that the beneficial effect of fullerene modification primarily originates from interactions at the buried perovskite interface. This interpretation is consistent with the SPV measurements, which reveal distinct interfacial charge-selective behaviors among the fullerene derivatives, with C60 and PCBM facilitating electron extraction while ICBA exhibits a different interfacial response.

Considering that fullerene derivatives exhibit finite solubility in perovskite precursor solutions, it is possible that a fraction of these molecules can partially dissolve in the precursor and redistribute during film crystallization. This raises the possibility that introducing fullerene derivatives directly into the perovskite precursor could generate an interfacial environment similar to that produced by intentional buried-interface modification. To examine this possibility, we incorporated C_{60}, PCBM, and ICBA directly into the perovskite precursor solution at a concentration of 0.5 mg mL^{-1}. Among these additives, ICBA produced the most pronounced enhancement in photovoltaic performance (Figure 1e,f and Figure S4). As summarized in Table 1, ICBA-additive devices achieved the highest average power conversion efficiency (21.8, ± 0.4 %) and the best-performing device reached 22.7%, outperforming the reference (20.1%) and other fullerene-based devices (19.8% for PCBM and 16.0% for C_{60}). This improvement was accompanied by a higher V_{OC} (0.88 V), superior fill factor (78.8%), and increased short-circuit current density J_{SC} (32.6 mA cm^{-2}), indicating that ICBA enhances both charge extraction and interfacial passivation. Figure 1f and Table S3 further confirm the improved photocurrent generation of the ICBA-based device, which exhibits the highest EQE-integrated J_{SC} among all fullerene additives, in good agreement with the corresponding *J–V* measurement.

The forward and reverse *J–V* scans of the devices are presented in Figure S5 and summarized in Table S4, showing that the ICBA-based device exhibits reduced hysteresis compared to the reference device. Interestingly, the overall photovoltaic characteristics closely resemble those observed in devices employing a buried fullerene interlayer. To verify whether the precursor-introduced fullerenes indeed modify the buried interface, rather than inferring this from device metrics, we directly characterized the energetics of the buried perovskite surfaces, as discussed below.

To directly examine whether precursor incorporation modifies the electronic structure of the actual buried surface, APS was performed on the peeled buried surfaces of the reference and fullerene-treated perovskite films (Figure 1g and Figure S6). The HOMO level of the reference buried surface was −5.2 eV, whereas those of the ICBA-, PCBM-, and C60-treated films were −5.0, −5.1, and −5.4 eV, respectively. The ICBA-treated buried surface therefore exhibits the closest alignment with the HOMO level of PEDOT:PSS (−5.0 eV), providing a more favorable energetic configuration for hole collection. Notably, these buried-surface HOMO levels (−5.0 to −5.4 eV) differ markedly from those of the neat fullerene films (−5.8 to −6.0 eV), arguing against the formation of a continuous fullerene layer at the buried interface. Instead, the results suggest that holes are extracted through an electronically modified perovskite surface rather than through a distinct fullerene phase. The possible chemical origin of this energetic modification, particularly the upward shift of the buried-surface HOMO following ICBA incorporation, is discussed later based on the interfacial XPS analysis.

Further insights into the charge carrier dynamics were obtained from transient photovoltage (TPV), transient photocurrent (TPC), V_{OC} as a function of light intensity, capacitance–voltage (*C–V*), and Mott-Schottky analysis (Figures S7,S8 and Table S5). The ICBA-treated device exhibited the longest carrier lifetime in the TPV measurements (τ = 5.24μs), indicating effective suppression of interfacial non-radiative recombination. These results consistently indicate that ICBA suppresses interfacial recombination and prolongs carrier lifetime, which together contribute to the observed performance enhancement. The TPC results showed that the ICBA-treated device exhibited the fastest carrier extraction dynamics ($\tau \approx 0.32$ μs), which correlated with its highest fill factor, likely due to reduced series resistance and more efficient charge collection under short-circuit conditions. The V_{OC} versus light intensity plots revealed that ICBA achieved the highest photovoltage under varying illumination, consistent with reduced trap-assisted recombination. Additionally, the Mott-Schottky analysis, in which the linear fit was restricted to the depletion regime of the $1/C^2$-V plot, indicated an increased built-in potential for the ICBA-treated device (0.77 V vs. 0.69 V for the reference), reflecting improved interfacial energetics and enhanced charge separation.

Taken together, the APS and carrier-dynamics results indicate that ICBA improves device performance by electronically modifying the perovskite buried surface, suppressing interfacial recombination, and facilitating charge collection, rather than by serving as a continuous hole-transporting fullerene layer.

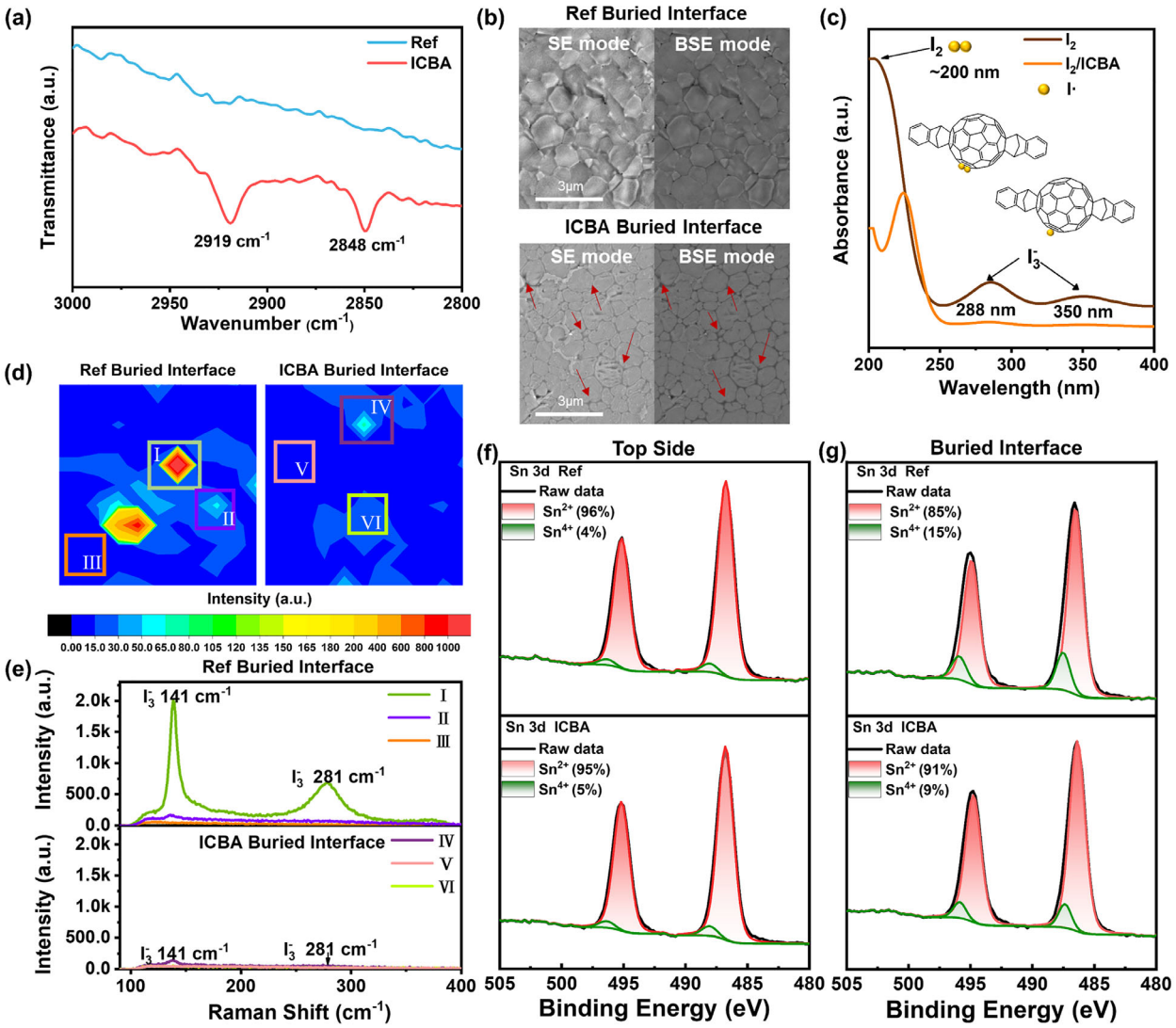

FIGURE 2 | (a) FTIR spectra of reference and ICBA-treated perovskite films, highlighting changes in vibrational features. (b) Top-view SEM image of the perovskite structure detached from the glass substrate, probed by secondary electron (SE) and backscattered electron (BSE) modes. (c) Schematic illustration of the iodine/polyiodide (I_2/I_3^-) capture mechanism induced by ICBA at the buried interface, along with the UV-Vis absorption spectra of ICBA powder dispersed in an aqueous I_2 solution. (d) Raman intensity mapping of the 141 cm^{-1} vibrational mode associated with I_3^- species over a 10×10 μm^2 area. (e) Raman spectra extracted from (d), comparing the signal regions of the reference and ICBA-treated films, highlighting the reduced I_3^- vibrational mode intensity upon ICBA incorporation. High-resolution XPS spectra of Sn 3d (f) top side and (g) buried interface, comparing the chemical states of perovskite films with and without ICBA.

2.2 | Distribution of ICBA at the Buried Interface

To determine the spatial distribution of ICBA within the Sn-Pb perovskite films, we employed a previously developed film-peeling technique to investigate the buried interface within the Sn—Pb perovskite films (Figure S9) [15, 17]. With this method, the buried perovskite-PEDOT:PSS interface can be comprehensively characterized in terms of morphology and chemical composition using a combination of SEM, AFM, FTIR, and XPS. Fourier-transform infrared (FTIR) spectroscopy was used in the attenuated total reflection (ATR) mode to detect ICBA-specific chemical signals. As depicted in Figure 2a, distinct absorption peaks at 2919 and 2848 cm^{-1}, attributed to the C—H stretching modes of ICBA (see pristine ICBA thin film in Figure S10), are clearly observed at the buried interface of the ICBA-treated film, whereas these features are absent in the reference film. These results suggest the presence of ICBA at the buried interface during film formation. Moreover, to verify that the ATR-FTIR signals originate from the buried perovskite surface rather than the underlying PEDOT:PSS layer, we measured the FTIR spectrum of a pristine PEDOT:PSS film (Figure S10b). The characteristic PEDOT:PSS vibrational bands at ~1187 cm^{-1} (S—O stretching) and ~837 cm^{-1} (C—S vibration) are absent in both peeled-interface spectra, confirming negligible interference from residual PEDOT:PSS. These results therefore confirm that the detected ICBA signals originate exclusively from the buried perovskite surface.

To directly determine the vertical distribution of ICBA within the perovskite films, time-of-flight secondary ion mass spectrometry

(ToF-SIMS) depth profiling was performed (Figure S11). The depth profiles were obtained by monitoring the characteristic C_9^- fullerene fragment together with PbI_2^-, SnI_2^-, $C_8H_8O_3S^-$ (PEDOT:PSS), and FTO signals. Compared with the reference sample, the ICBA-treated film exhibits a clear enrichment of the C_9^- signal at the PEDOT:PSS/perovskite buried interface, providing direct evidence for the preferential accumulation of ICBA. These results are in agreement with the ATR-FTIR measurements of the peeled buried interface.

Having confirmed the preferential enrichment of ICBA at the buried interface, we next examined whether this spatial distribution was accompanied by changes in the buried-interface morphology using SEM. The SEM images (Figure S12a) showed negligible morphological differences between the reference and ICBA-treated films under both SE and BSE conditions, suggesting no significant surface modification by ICBA. However, as shown in Figure 2b, SEM images of the buried interface samples under the SE mode revealed that ICBA-treated films exhibited a more uniform surface morphology than the reference. Moreover, top-view BSE images of the buried interface exhibited distinct darker contrast areas at grain boundaries exclusively in the ICBA-treated films, as indicated by the red arrows in Figure 2b. The lower backscattering intensity at these grain boundaries confirms ICBA localization, as its organic composition leads to weaker electron scattering compared to heavy elements, such as Pb, in perovskite. This localization likely contributes to passivation at grain boundaries.

To further assess the surface morphology, atomic force microscopy (AFM) was conducted on both the top and bottom interfaces (Figure S13). The roughness values (Ra) remained comparable between the reference and ICBA-treated films at both interfaces. The top-surface Ra changed slightly from 21.59 to 23.42 nm, whereas the buried-interface Ra varied marginally from 14.93 to 15.11 nm, indicating that ICBA does not significantly alter the overall surface roughness or surface topography. In contrast, FTIR (Figure 2a) and TOF-SIMS (Figure S11) confirm the preferential accumulation of ICBA at the buried interface, while the SEM observations (Figure 2b) reveal a more uniform buried-interface morphology. Together, these results suggest that ICBA primarily modifies the buried interface through localized chemical accumulation rather than large-scale morphological changes.

2.3 | Iodine Scavenging and Chemical Stabilization Effects of ICBA

Having established that ICBA preferentially accumulates at the buried interface, we next sought to identify the chemical origin of its stabilizing effect. Because molecular iodine (I_2) is the key oxidant driving Sn^{2+} oxidation in Sn-Pb perovskites, we first examined whether ICBA can directly interact with iodine species. To this end, UV-vis absorption spectra of an aqueous I_2 solution were recorded before and after mixing with ICBA (Figure 2c). The UV-vis absorption spectra (Figure 2c) show a clear reduction in the intensity of the characteristic I_2 absorption peak at ~200 nm and those of I_3^- at 288 and 350 nm upon mixing with ICBA. This spectral suppression suggests that ICBA effectively interacts with molecular iodine, likely through charge-transfer complexation or chemical binding, thereby reducing the concentration of free I_2 and its derivatives in the solution [18]. Given the electron-rich indene moieties in ICBA, the molecule can act as a mild electron donor, forming a ground-state charge-transfer complex with electrophilic I_2, as widely documented for I_2 with electron-donating molecules [18]. Such complexation is consistent with a reduced concentration and chemical activity of free I_2, consistent with the diminished I_2 absorption features observed upon mixing (Figure 2c). Furthermore, the reduced absorption at ~288 and 350 nm suggests that ICBA also suppresses the formation or stability of I_3^-, a product typically arising from I^- and I_2 reaction [14, 30]. These observations imply that the I_2 is either directly bound to ICBA or otherwise sequestered in a form that limits its participation in further redox reactions. To examine whether this behavior is unique to ICBA, analogous UV-vis measurements were also performed for PCBM and C_{60} (Figure S14). Similar changes in the iodine absorption spectra were observed for both fullerene derivatives, indicating that the interaction with iodine is a general characteristic of fullerene derivatives rather than being exclusive to ICBA.

To verify whether this iodine-scavenging behavior also occurs in the perovskite films, Raman spectroscopy was performed to probe iodine-related species at the buried interface of the perovskite layer. As shown in Figure 2d, the Raman intensity mapping of the 141 cm^{-1} vibrational mode, which is characteristic of I_3^- species, was carried out over a 10 × 10 μm^2 area [18]. The reference device exhibited significantly stronger localized Raman signals compared to the ICBA-treated device, indicating a higher accumulation of I_3^- at the buried interface. The corresponding normalized spectra in Figure 2e show prominent peaks at 141 and 281 cm^{-1}, both assigned to I_3^- vibrational modes. These features were markedly suppressed in the ICBA-treated film, suggesting that ICBA effectively reduces the concentration of interfacial iodine species. This suppression supports the proposed iodine-scavenging function of ICBA and its role in inhibiting I_3^- formation, thereby mitigating Sn^{2+} oxidation and improving interfacial stability. In addition to the UV-vis data and buried interface Raman analysis, these results allow us to conclude that ICBA plays a dual role in chemical passivation and interfacial stabilization.

If ICBA indeed suppresses iodine species, a corresponding reduction in Sn oxidation should also be observed. Therefore, XPS was performed to examine the oxidation state of Sn in the perovskite films. The Sn 3d spectra for both the reference and ICBA-modified samples, at both the top surface and buried interface, exhibited slightly asymmetric line shapes. These were deconvoluted into doublets corresponding to the $3d_{5/2}$ and $3d_{3/2}$ peaks for both Sn^{2+} and Sn^{4+} oxidation states. For the buried interface of the ICBA-modified film, the Sn $3d_{5/2}$ peaks appeared at 486.4 and 487.4 eV, corresponding to Sn^{2+} and Sn^{4+}, respectively [31]. The reference sample showed nearly identical positions at 486.5 and 487.5 eV. On the top surfaces, a slight shift to higher binding energies was observed.

Peak area analysis of the buried interface revealed a reduction in Sn^{4+} content from 15% in the reference to 9% in the ICBA-treated film (Figure 2g and Table S6), indicating that ICBA suppresses the oxidation of Sn^{2+} and chemically stabilizes the buried interface [32, 33]. Importantly, this chemical stabilization also accounts

for the buried-surface energetics observed in Figure 1g. Oxidized species such as Sn^{4+} and iodine-related defects are known to increase the surface ionization energy of Sn-based perovskites [34], and their suppression by ICBA therefore explains, at least in part, the upward shift of the buried-surface HOMO towards the work function of PEDOT:PSS.

In contrast, the top-surface spectra (Figure 2f and Table S7) showed negligible differences between the two samples, confirming that ICBA's passivation effect is localized at the buried interface. Notably, the Sn^{4+} content at the top surface of both films was significantly lower (~5%) than that at the buried interface. This is attributed to the fact that the buried interface is in direct contact with the acidic PEDOT:PSS HTL, which can facilitate the oxidation of Sn^{2+} to Sn^{4+}. The lack of such exposure at the top surface explains the reduced oxidation state [35, 36].

2.4 | Optical Characterization and Photophysical Properties

Having established that ICBA suppresses iodine-induced chemical degradation at the buried interface, we next investigated how this chemical stabilization influences the optoelectronic properties of the perovskite films using steady-state photoluminescence (PL) measurements. As shown in Figure 3a, the ICBA-treated film exhibited significantly enhanced PL intensity compared to the reference, indicating a lower non-radiative recombination rate. This observation agreed with the time-correlated single-photon counting (TCSPC) results shown in Figure 3b and Table S8, revealing that the fast decay constant (τ_1), representing carrier trapping by deep defects, increased from 5.03 (Ref) to 5.53 μs (ICBA). More notably, the slow decay constant (τ_2), related to bimolecular recombination, improved from 14.07 to 22.91 μs. These results indicate that ICBA suppresses trap formation and extends carrier lifetime, an effect that cannot be solely attributed to surface passivation but is more likely associated with the suppression of chemical degradation pathways during thermal annealing.

To directly probe the effect of ICBA on interfacial carrier dynamics, femtosecond transient absorption (fs-TAS) spectroscopy was performed on the PEDOT:PSS/perovskite structures (Figure S15 and Table S9). Both the reference and ICBA-treated films exhibit similar transient spectral features, consisting of a photo-induced bleaching (PIB) signal below 975 nm and a photo-induced absorption (PIA) signal above 975 nm. While the sub-picosecond dynamics are nearly identical, indicating comparable hot-carrier cooling, the ICBA-treated film exhibits a faster recovery of the integrated PIB signal after ~50 ps. Kinetic fitting further confirms the accelerated PIB recovery in the ICBA-treated film, consistent with more efficient hole extraction across the buried interface. These results provide direct spectroscopic evidence supporting the improved charge extraction induced by precursor-engineered ICBA.

We next employed space-charge-limited current (SCLC) measurements in hole-only device structures to quantitatively evaluate the effect of ICBA on trap densities and hole mobility (Figure 3c, Figure S16 and Table S10). The ICBA-treated film exhibited a reduced trap density and enhanced hole mobility compared to the reference, reaffirming ICBA's effectiveness in suppressing intrinsic defect formation and improving charge transport.

These improvements are consistent with the stronger XRD reflections (Figure S17). The dominant reflections at ~14° and ~28°, together with the weak higher-angle peaks shown in the enlarged view, are characteristic of highly oriented mixed Sn-Pb perovskite films. XPS analysis (Figure 2g and Figure S18) reveals that ICBA-treated films exhibit lower binding energies in both the I 3d and Sn 3d spectra, suggesting a reduction in I_2 accumulation and mitigation of Sn^{2+} oxidation to Sn^{4+}. These findings imply that ICBA not only stabilizes halide ions through charge-transfer interactions but may also help maintain the reduced oxidation state of Sn during perovskite crystallization. This chemical stabilization likely reduces defect generation at grain boundaries and interfaces, ultimately leading to improved optoelectronic properties.

To assess the spatial uniformity of the optoelectronic quality and estimate the upper limit of the achievable open circuit voltage (V_{OC}), we employed hyperspectral PL mapping to derive the quasi-Fermi level splitting (QFLS) across the film (Figure 3d–f and Table S11). This technique enables the visualization of local variations in non-radiative recombination and provides insights into the electronic landscape under steady-state conditions, which is particularly relevant for evaluating half-cell performance [37]. A schematic of the hyperspectral PL imaging system used in this study is shown in Figure S19.

Figure 3d shows the hyperspectral PL image of the glass/PEDOT:PSS/perovskite stack at a 970 nm emission wavelength, revealing significantly stronger PL emission intensity in the ICBA-treated film than in the reference, suggesting reduced non-radiative recombination. The spatial QFLS maps shown in Figure 3e reveal that the ICBA-treated perovskite film maintains a higher and more uniform quasi-Fermi level splitting (0.91 ± 0.11 eV), indicative of reduced non-radiative losses and more homogeneous optoelectronic quality. This is in line with the higher V_{OC} obtained in ICBA-based devices in Figure 1e,f relative to reference cells. Figure 3f displays the Urbach energy (E_U) distribution, which reflects energetic disorder; the ICBA-treated perovskite sample shows a narrower E_U distribution and a slight reduction (~1 meV) in the average E_U, pointing to a suppressed sub-bandgap tail state. The detailed calculation of the average E_U is shown in the Methods section in the Supporting Information. Taken together, these results indicate that ICBA plays a multifunctional role in tuning interfacial energetics and mitigating degradation pathways, especially the oxidation of Sn^{2+} during thermal annealing, which contributes to improved film uniformity, reduced defect density, and enhanced optoelectronic performance.

2.5 | Operational and Shelf Stability of ICBA-Modified Devices

The above characterizations consistently indicate that ICBA suppresses chemical degradation, reduces defect formation, and improves charge transport. We therefore next evaluated whether these material-level improvements translate into enhanced operational and storage stability. Maximum power point tracking

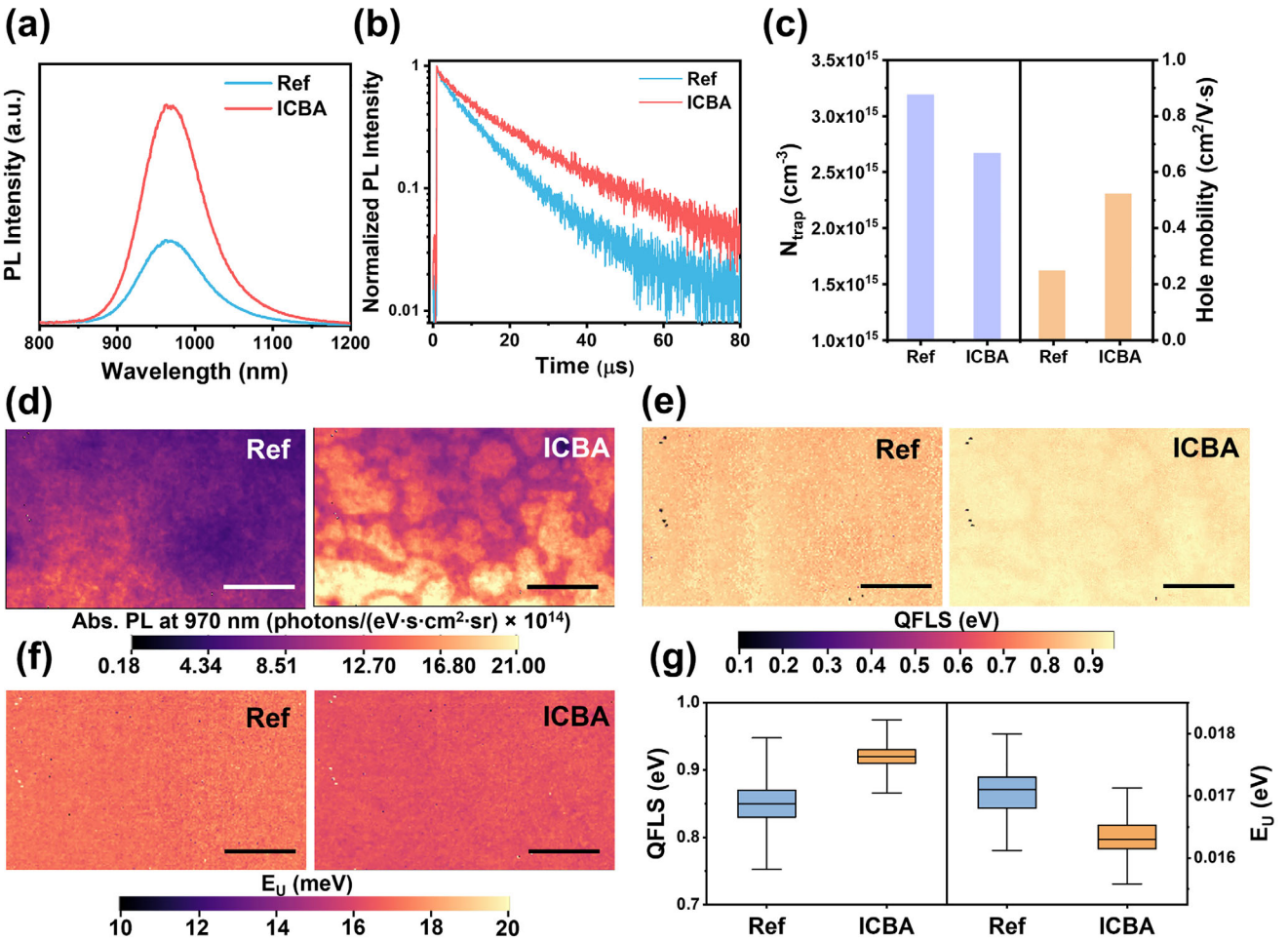

FIGURE 3 | (a) Photoluminescence spectra of the glass/perovskite layer without and with ICBA. (b) Time-correlated single-photon counting (TCSPC) spectroscopy of perovskite films without and with ICBA. (c) Space charge-limited current (SCLC) measurements of hole-only devices with the structure ITO/PEDOT:PSS/perovskite/MoO_3/Ag. (d) Hyperspectral PL image of the glass/PEDOT:PSS/Perovskite stack. Scale bar: 50 μm. (e) Quasi-Fermi level splitting (QFLS) maps of the reference and ICBA-treated films. Scale bar: 50 μm. (f) Urbach energy (E_U) distribution maps for both samples. Scale bar: 50 μm. (g) Average values of QFLS and E_U. The box range spans from the 25th to 75th percentiles, the center line represents the median, and the whiskers comprise 1.5 × the interquartile range.

was performed on encapsulated devices under continuous 1-sun LED illumination in ambient air at 25°C. As shown in Figure 4a, the ICBA-treated device retained approximately 88% of its initial efficiency after 300 h of continuous operation, whereas the reference device progressively decreased to approximately 68%. This enhancement could be attributed to the suppressed formation of molecular iodine [18], which is known to accelerate the degradation of perovskites. The preferential accumulation of ICBA at the buried interface plays a key role in chemically and electronically stabilizing this critical region, thereby mitigating photoinstability.

In addition, the long-term storage stability shown in Figures 4b,c highlights the distinct advantage of ICBA in suppressing intrinsic degradation pathways under inert conditions. The photovoltaic parameters of the aged devices are listed in Table S12. While the reference device exhibited progressive losses in current density and fill factor over 2496 h, with J_{SC} decreasing from 30.6 to 25.0 mA cm^{-2} and fill factor dropping from 76.0% to 74.6% after 2496 h, the ICBA-treated device retained most of its initial performance. This improved shelf stability can be correlated with reduced iodide migration and diminished molecular iodine formation, both of which are known contributors to perovskite decomposition, even in dark, inert environments [18, 38]. The incorporation of ICBA at the buried interface likely creates a more chemically stable interfacial region by acting as a diffusion barrier and iodine scavenger, thereby minimizing detrimental redox reactions at the perovskite/HTL interface. This hypothesis is further supported by the spatially resolved characterization and interfacial analysis discussed in earlier sections, which confirmed the preferential accumulation of ICBA at the bottom side of the perovskite layer. In addition, the preferential accumulation of ICBA at the buried interface may also act as a physical barrier, limiting direct contact between the perovskite and PEDOT:PSS, thereby further mitigating interfacial degradation.[39] Such targeted interface modification provides a rational strategy for improving the intrinsic material stability of mixed Sn—Pb perovskites.

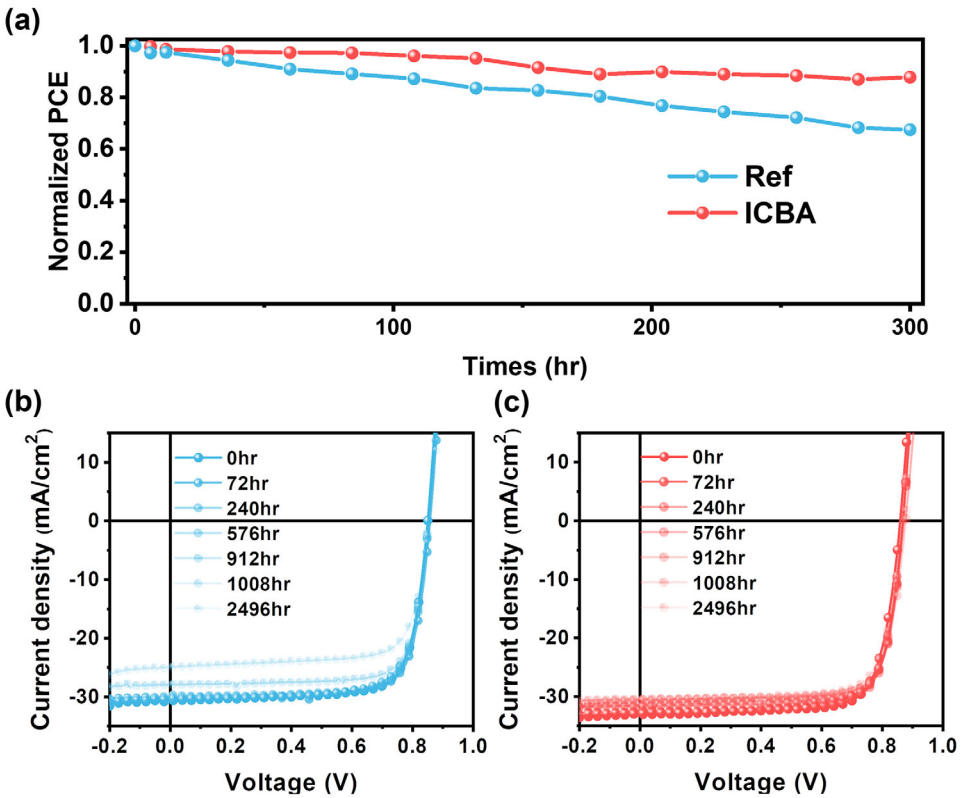

FIGURE 4 | (a) Maximum power point (MPP) tracking of encapsulated reference and ICBA-treated devices under continuous 1-sun LED illumination in ambient air at 25°C. The devices were continuously operated at their respective MPPs throughout the measurement. Fresh *J–V* scans were recorded every 6 h during the first 24 h and every 24 h thereafter to update the device efficiency. (b,c) *J–V* characteristics of Sn–Pb PSCs with and without ICBA additive. The devices were stored in a nitrogen-filled glovebox and periodically measured using a 1-sun solar simulator.

3 | Conclusion

In this study, we established ICBA as a multifunctional interfacial regulator for narrow-bandgap Sn–Pb perovskite solar cells. In addition to its favorable energy-level alignment, ICBA selectively suppresses interfacial electron extraction while maintaining efficient hole transport, making it particularly suitable for inverted architectures, in which buried-interface recombination dominates. Spectroscopic and structural analyses revealed the preferential localization of ICBA at the buried interface and grain boundaries, where it chemically interacts with iodine species and suppresses Sn^{2+} oxidation. This coupled electronic and chemical stabilization reduces trap formation and energetic disorder, leading to enhanced photophysical properties and reduced voltage losses. As a result, ICBA-modified devices achieved efficiencies exceeding 22% and exhibited markedly improved storage stability, retaining over 93% of their initial performance after 2496 h in nitrogen. Collectively, these findings uncover a degradation pathway specific to interfacial regulation and provide mechanistic insights into stabilizing lead-reduced perovskite photovoltaics.

Acknowledgements

C.-T. L. thanks the National Science and Technology Council (114-2628-E-005 -001, 115-2927-I-005-502, 114-2634-F-005 -002), and Innovation and Development Center of Sustainable Agriculture from the Featured Areas Research Center Program within the framework of the Higher Education Sprout Project by the Ministry of Education (MOE) in Taiwan. T.J.M thanks the Royal Commission for the Exhibition of 1851 for their financial support through a Research Fellowship. T.J.M. acknowledges funding from a Royal Society University Research Fellowship (URF/R1/221834) and the Royal Society Research Fellows Enhanced Research Expenses (RF/ERE/221066). M.D. acknowledges funding received from the European Union's Horizon Europe research and innovation program under the Marie Sklodowska-Curie grant agreement No. 101103762. C.-T. L. and M.D. acknowledge the mobility grant received from the National Science and Technology Council (115 -2927-I-005 -502 -) and the Hungarian Academy of Sciences (NKM2025-4/2025).

Conflicts of Interest

The authors declare no conflicts of interest.

Data Availability Statement

The data that support the findings of this study are available from the corresponding author upon reasonable request.

References

1. R. Wang, M. Mujahid, Y. Duan, Z. K. Wang, J. Xue, and Y. Yang, "A Review of Perovskites Solar Cell Stability," *Advanced Functional Materials* 29 (2019): 1808843, https://doi.org/10.1002/adfm.201808843.

2. J. Y. Kim, J. W. Lee, H. S. Jung, H. Shin, and N. G. Park, "High-Efficiency Perovskite Solar Cells," *Chemical Reviews* 120, no. 15 (2020): 7867–7918, https://doi.org/10.1021/acs.chemrev.0c00107.

3. A. K. Jena, A. Kulkarni, and T. Miyasaka, "Halide Perovskite Photovoltaics: Background, Status, and Future Prospects," *Chemical Reviews* 119, no. 5 (2019): 3036–3103, https://doi.org/10.1021/acs.chemrev.8b00539.

4. W. Zhang, H. Yuan, X. Li, et al., "Component Distribution Regulation in Sn-Pb Perovskite Solar Cells Through Selective Molecular Interaction," *Advanced Materials* 35, no. 39 (2023): 2303674, https://doi.org/10.1002/adma.202303674.

5. J. Wang, M. A. Uddin, B. Chen, et al., "Enhancing Photostability of Sn-Pb Perovskite Solar Cells by an Alkylammonium Pseudo-Halogen Additive," *Advanced Energy Materials* 13, no. 15 (2023): 2204115, https://doi.org/10.1002/aenm.202204115.

6. D.-T. Wu, W.-X. Zhu, Y. Dong, et al., "Enhancing the Efficiency and Stability of Tin-Lead Perovskite Solar Cells via Sodium Hydroxide Dedoping of PEDOT:PSS," *Small Methods* 8 (2024): 2400302, https://doi.org/10.1002/smtd.202400302.

7. S.-E. Hsu, W.-X. Zhu, D.-T. Wu, et al., "Reducing optical reflection loss Through textured PEDOT:PSS in hybrid Sn–Pb perovskite solar cells," *Sustainable Energy & Fuels* 8, no. 8 (2024): 1712–1718, https://doi.org/10.1039/D4SE00029C.

8. Y. Dong, W. X. Zhu, D. T. Wu, et al., "Crystal Growth Modulation of Tin–Lead Halide Perovskites via Chaotropic Agent," *Journal of the American Chemical Society* 147, no. 35 (2025): 31578–31590, https://doi.org/10.1021/jacs.5c05772.

9. S. Lee, M. Y. Woo, C. Kim, et al., "Buried Interface Modulation via PEDOT:PSS Ionic Exchange for the Sn-Pb Mixed Perovskite Based Solar Cells," *Chemical Engineering Journal* 479 (2024): 147587, https://doi.org/10.1016/j.cej.2023.147587.

10. T. J. Macdonald, L. Lanzetta, X. Liang, D. Ding, and S. A. Haque, "Engineering Stable Lead-Free Tin Halide Perovskite Solar Cells: Lessons From Materials Chemistry," *Advanced Materials* 35, no. 25 (2023): 2206684, https://doi.org/10.1002/adma.202206684.

11. L. Lanzetta, T. Webb, J. M. Marin-Beloqui, T. J. Macdonald, and S. A. Haque, "Halide Chemistry in Tin Perovskite Optoelectronics: Bottlenecks and Opportunities," *Angewandte Chemie International Edition* 62, no. 8 (2023): 202213966, https://doi.org/10.1002/anie.202213966.

12. L. Lanzetta, T. Webb, N. Zibouche, et al., "Degradation Mechanism of Hybrid Tin-Based Perovskite Solar Cells and the Critical Role of Tin (IV) Iodide," *Nature Communications* 12, no. 1 (2021): 2853, https://doi.org/10.1038/s41467-021-22864-z.

13. L. Lanzetta, H. Hernandez, B. Vishal, et al., "Tin–Lead Perovskite Solar Cells With Enhanced Reverse Bias Stability," *ACS Energy Letters* 10, no. 5 (2025): 2093–2095, https://doi.org/10.1021/acsenergylett.5c00727.

14. A. Alsulami, L. Lanzetta, L. Huerta Hernandez, et al., "Triiodide Formation Governs Oxidation Mechanism of Tin–Lead Perovskite Solar Cells via A-Site Choice," *Journal of the American Chemical Society* 146, no. 33 (2024): 22970–22981, https://doi.org/10.1021/jacs.4c01919.

15. H. Y. Lin, Z. Jiang, S. C. Liu, et al., "Overcoming Microstructural Defects at the Buried Interface of Formamidinium-Based Perovskite Solar Cells," *ACS Applied Materials & Interfaces* 16, no. 36 (2024): 47763–47772, https://doi.org/10.1021/acsami.4c11052.

16. X. Yang, D. Luo, Y. Xiang, et al., "Buried Interfaces in Halide Perovskite Photovoltaics," *Advanced Materials* 33, no. 7 (2021): 2006435, https://doi.org/10.1002/adma.202006435.

17. S. C. Liu, H. Y. Lin, S. E. Hsu, et al., "Highly Reproducible Self-Assembled Monolayer Based Perovskite Solar Cells via Amphiphilic Polyelectrolyte," *Journal of Materials Chemistry A* 12, no. 5 (2024): 2856–2866, https://doi.org/10.1039/d3ta04512a.

18. X. Ren, J. Wang, Y. Lin, et al., "Mobile Iodides Capture for Highly Photolysis- and Reverse-Bias-Stable Perovskite Solar Cells," *Nature Materials* 23, no. 6 (2024): 810–817, https://doi.org/10.1038/s41563-024-01876-2.

19. W. Xu, L. J. F. Hart, B. Moss, et al., "Impact of Interface Energetic Alignment and Mobile Ions on Charge Carrier Accumulation and Extraction in p-i-n Perovskite Solar Cells," *Advanced Energy Materials* 13 (2023): 2301102, https://doi.org/10.1002/aenm.202301102.

20. Y. Sun, Y. Lai, and Y. Yang, "Progress of Hole-Transport Layers in Mixed Sn-Pb Perovskite Solar Cells," *Small* 20 (2024): 2406991, https://doi.org/10.1002/smll.202406991.

21. Y. Dong, F. M. Rombach, G. Min, et al., "Dopant-Induced Interactions in Spiro-OMeTAD: Advancing Hole Transport for Perovskite Solar Cells," *Materials Science and Engineering: R: Reports* 162 (2025): 100875, https://doi.org/10.1016/j.mser.2024.100875.

22. Z. Jiang, T. Du, C.-T. Lin, et al., "Deciphering the Role of Hole Transport Layer HOMO Level on the Open Circuit Voltage of Perovskite Solar Cells," *Advanced Materials Interfaces* 10, no. 19 (2022): 2201737, https://doi.org/10.1002/admi.202201737.

23. H. Kim, J. W. Lee, G. R. Han, et al., "Highly Efficient Hole Transport Layer-Free Low Bandgap Mixed Pb–Sn Perovskite Solar Cells Enabled by a Binary Additive System," *Advanced Functional Materials* 32, no. 12 (2022): 2110069, https://doi.org/10.1002/adfm.202110069.

24. C.-T. Lin, S. Pont, J. Kim, et al., "Passivation Against oxygen and light induced degradation by the PCBM electron transport layer in planar perovskite solar cells," *Sustainable Energy & Fuels* 2, no. 8 (2018): 1686–1692, https://doi.org/10.1039/c8se00095f.

25. J. Seo, S. Park, C. Kim, et al., "Benefits of Very Thin PCBM and LiF Layers For Solution-Processed p–i–n Perovskite Solar Cells," *Energy & Environmental Science* 7, no. 8 (2014): 2642–2646, https://doi.org/10.1039/c4ee01216j.

26. N. B. Kotadiya, A. Mondal, P. W. M. Blom, D. Andrienko, and G. J. A. H. Wetzelaer, "A Window to Trap-Free Charge Transport in Organic Semiconducting Thin Films," *Nature Materials* 18 (2019): 1182–1186, https://doi.org/10.1038/s41563-019-0473-6.

27. A. Tong, X. Chen, Z. Jin, et al., "The Overlooked Hole Transport Properties of Indene-C60 Bisadduct in $CsPbBr_3$ Perovskite Solar Cells," *Chemical Engineering Journal* 522 (2025): 167567, https://doi.org/10.1016/j.cej.2025.167567.

28. M. Daboczi, J. Kim, J. Lee, et al., "Towards Efficient Integrated Perovskite/Organic Bulk Heterojunction Solar Cells: Interfacial Energetic Requirement to Reduce Charge Carrier Recombination Losses," *Advanced Functional Materials* 30, no. 25 (2020): 2001482, https://doi.org/10.1002/adfm.202001482.

29. M. Daboczi, I. Hamilton, S. Xu, et al., "Origin of Open-Circuit Voltage Losses in Perovskite Solar Cells Investigated by Surface Photovoltage Measurement," *ACS Applied Materials & Interfaces* 11, no. 50 (2019): 46808–46817, https://doi.org/10.1021/acsami.9b16394.

30. T. Jiang, Z. Chen, X. Chen, et al., "Realizing High Efficiency Over 20% of Low-Bandgap Pb–Sn-Alloyed Perovskite Solar Cells by In Situ Reduction of Sn 4+," *Solar RRL* 4, no. 3 (2020): 1900467, https://doi.org/10.1002/solr.201900467.

31. S. Joy, H. R. Atapattu, S. Sorensen, et al., "How Additives for Tin Halide Perovskites Influence the Sn4+ Concentration," *Journal of Materials Chemistry A* 10, no. 25 (2022): 13278–13285, https://doi.org/10.1039/d2ta01429g.

32. T. Mahmoudi, W. Y. Rho, M. Kohan, Y. H. Im, S. Mathur, and Y. B. Hahn, "Suppression of Sn^{2+}/Sn^{4+} Oxidation in Tin-Based Perovskite Solar Cells With Graphene-Tin Quantum Dots Composites in Active Layer," *Nano Energy* 90 (2021): 106495, https://doi.org/10.1016/j.nanoen.2021.106495.

33. R. Nishikubo, N. Ishida, Y. Katsuki, A. Wakamiya, and A. Saeki, "Minute-Scale Degradation and Shift of Valence-Band Maxima of $(CH_3NH_3)SnI_3$ and $HC(NH_2)_2SnI_3$ Perovskites Upon Air Exposure," *Journal of Physical Chemistry C* 121, no. 36 (2017): 19650–19656, https://doi.org/10.1021/acs.jpcc.7b06294.

34. L. Chen, S. Fu, Y. Li, N. Sun, Y. Yan, and Z. Song, "On the Durability of Tin-Containing Perovskite Solar Cells," *Advanced Science* 11, no. 1 (2024): 2304811, https://doi.org/10.1002/advs.202304811.

35. B. Chen, Z. Yu, A. Onno, et al., "Bifacial All-Perovskite Tandem Solar Cells," *Science Advances* 8, no. 47 (2025): add0377, https://doi.org/10.1126/sciadv.add0377.

36. P. Caprioglio, M. Stolterfoht, C. M. Wolff, et al., "On the Relation Between the Open-Circuit Voltage and Quasi-Fermi Level Splitting in Efficient Perovskite Solar Cells," *Advanced Energy Materials* 9, no. 33 (2019): 1901631, https://doi.org/10.1002/aenm.201901631.

37. H. Back, G. Kim, J. Kim, et al., "Achieving Long-Term Stable Perovskite Solar Cells via Ion Neutralization," *Energy & Environmental Science* 9, no. 4 (2016): 1258–1263, https://doi.org/10.1039/c6ee00612d.

38. F. M. Rombach, A. Dasgupta, M. Kober-Czerny, et al., "Disentangling Degradation Pathways of Narrow Bandgap Lead-Tin Perovskite Material and Photovoltaic Devices," *Nature Communications* 16, no. 1 (2025): 5450, https://doi.org/10.1038/s41467-025-58489-9.

Supporting Information

Additional supporting information can be found online in the Supporting Information section.

Supporting File: adfm77758-sup-0001-SuppMat.pdf.